Performance analyses of a novel finned parabolic trough receiver with inner tube for solar cascade heat collection

LIU Peng[1,3], REN TingTing[1,3], GE YanLin[1,3], LIU Wei[2] & CHEN LinGen[1,3*]

[1] *Institute of Thermal Science and Power Engineering, Wuhan Institute of Technology, Wuhan 430205, China;*
[2] *School of Energy and Power Engineering, Huazhong University of Science and Technology, Wuhan 430074, China;*
[3] *School of Mechanical & Electrical Engineering, Wuhan Institute of Technology, Wuhan 430205, China*

Designing highly-efficient parabolic trough receiver (PTR) contributes to promoting solar thermal utilization and alleviating energy crisis and environmental problems. A novel finned PTR with inner tube (FPTR-IT), which can provide different grades of thermal energy with two heat transfer fluids (oil and water), is designed to improve thermal efficiency. In this FPTR-IT, an inner tube and straight fins are employed to respectively lessen heat loss at upper and lower parts of the absorber. Based on the design, a numerical model is developed to investigate its performance. Comparisons with other PTRs indicate that the FPTR-IT can combine the advantages of PTR with inner tube and finned PTR and obtain the best performance. Moreover, performance evaluation under broad ranges of direct normal irradiances (300–1000 W/m^2), flow rates (50–250 L/min) and inlet temperatures (400–600 K) of oil as well as flow rates (3.6–10 L/min) and inlet temperatures (298.15–318.15 K) of water is investigated. Compared with conventional PTR, heat loss is reduced by 20.7%–63.2% and total efficiency is improved by 0.03%–4.27%. Furthermore, the proportions of heat gains for water and oil are located in 8.3%–73.9% and −12.0%–64.3%, while their temperature gains are located in 11.6–37.9 K and −1.2–19.6 K, respectively. Thus, the proposed FPTR-IT may have a promising application prospect in remote arid areas or islands to provide different grades of heat for electricity and freshwater production.

finned parabolic trough receiver, inner tube, heat loss, total efficiency, solar cascade heat collection, performance analyses

1   Introduction

Exploitation and utilization of solar energy have a good perspective for reducing dependence on fossil energy and realizing the carbon peaking and carbon neutrality goals of China due to its abundance and cleaning properties. Solar thermal utilization is a promising way to provide heat source for living and production processes, including electricity generation from concentrating solar power (CSP) [1–5], concentrating photovoltaic/concentrating solar power (CPV/ CSP) [6,7], desalination [8–10], solar thermochemical re-

actor [11–13], domestic heating [14,15], etc. Solar collectors are the key components for solar thermal utilization, which can absorb solar irradiance and generate heat. Among them, parabolic trough collector (PTC), which has advantages of modularity and easy to match with other renewable energy sources, is widely used in practical applications [16]. Nevertheless, conventional parabolic trough receiver (CPTR, see Figure 1(a)) in a PTC suffers extremely circumferential non-uniform heat flux due to upper and lower parts of absorber being illumined by direct and concentrated irradiances, respectively. This may lead to extremely high maximum temperature, as well as large temperature gradient, thermal stress and heat loss, and consequently brings huge

challenges to the PTC's safe and efficient operation [17,18]. Therefore, technologies and designs for reducing temperature, thermal stress and heat loss are highly needed.

Recently, substantial efforts have been devoted to developing highly efficient PTC [19–22]. Heat loss lessening technologies and heat transfer enhancement techniques are two main methods to promote receiver efficiency. The former is concentrated on restraining the heat loss through radiation from absorber to glass cover, such as selective coatings [23], radiation shields [24,25]. Zhao et al. [26] have proposed a good strategy that using several selective-absorbing coatings along flow direction and they managed to debase heat loss by 29.3% and improve thermal efficiency by 4.3%. Recently, Yang et al. [27] found that heat loss through radiation may surpass absorbed heat from solar irradiance in directly illumined zone at upper part of absorber, especially at high heat transfer fluid (HTF) temperature and low direct normal irradiance (DNI). Thus, a negative thermal-flux occurs in this region. A radiation shield between glass cover and absorber at the directly illumined zone was proposed by Wang et al. [28] to lessen heat loss through overcoming negative thermal-flux region. The results of tests showed that compared with CPTR, the PTR with metal radiation shield can obviously decline heat loss by 28.1% under absorber temperature of 600°C. Nevertheless, some of direct irradiance would be intercepted by the metal radiation shield and thus the optical efficiency be inevitably downgraded. As a result, the PTR with metal radiation shield could even achieve lower thermal efficiency than CPTR under low temperature of HTF and high DNI. To this end, some excellent strategies have been proposed, such as replacing the metal radiation shield with glass shields [29] or solar-transparent aerogel [30,31]. The results indicated that these strategies can mitigate the interception of direct irradiance and effectually improve the thermal efficiency under broad ranges of DNI and temperature of HTF. However, as the heat loss lessening technologies did not decline the temperature of the absorber, the PTR could still suffer extremely high temperature, temperature gradient and thermal stress.

Unlike heat loss lessening technologies, heat transfer enhancement techniques, including nanofluids [32–35] and turbulators [16,36,37], were concentrated on strengthening the heat transfer coefficient of HTF so as to prevent excessive temperature and heat loss of absorber. Though nanofluids, which can improve thermal properties of base fluid by adding and dispersing nanoparticles, have great potential for promoting highly efficient PTR and attract wide research interests, overcoming their weaknesses of high production cost, agglomeration and instability still remain an ongoing challenge in industrial application [32,34]. Turbulators applied in traditional heat exchanger [38,39] could enhance the heat transfer coefficient through augmenting fluid mixing, which provides a promising method for improving perfor-

mance of PTR. Until now, many turbulators, such as dimpled tube [40], corrugated tube [41], finned tube [42–44], ribbed tube [45], wavy tube [46], porous inserts [47,48], conical strip [49], twisted tape [50], metal foams [51], longitudinal vortex generators [52], rotary receiver [53], have been investigated and analyzed for developing highly efficient PTR. Biswakarma et al. [54] reported a performance analysis of an internally helically V-grooved absorber and obtained 41.3% enhancement in heat transfer coefficient. Shi et al. [55] employed a helically convex absorber tube for enhancing heat transfer of PTR. They found that compared with CPTR, 34% improvement in heat transfer performance is obtained. Liu et al. [56] proposed a ribbed absorber tube and conducted a multi-objective optimization. They found that the ribbed absorber could achieve 57%–255% and 2.2% improvement in heat transfer and thermal efficiency, respectively. Bellos et al. [57] have evaluated a finned PTR (FPTR, see Figure 1(b)) through simulation. They found that compared with CPTR, the FPTR obtains 65.8% and 0.82% improvement in heat transfer and thermal efficiency but assumes double pressure losses. However, the turbulators are not suitable for PTR under large flow rate (FR) conditions because the gains in thermal efficiency are offset by the large pumping power consumption (PPC). Moreover, though the turbulators are able to strengthen heat transfer between absorber and HTF, they cannot suppress the negative thermal-flux region and even deprave the performance under high temperature of HTF. Lately, a strategy of PTR with inner tube (PTR-IT, see Figure 1(c)) was proposed by Liu et al. [58]. In this strategy, an inner tube is tightly attached to the directly illumined zone with low temperature HTF (seawater or water) flowing through it to conquer the negative thermal-flux region as well as provide low temperature heat source for desalination or domestic heating. They found that heat loss is decreased by 33.1%–50.1% and total efficiency is enhanced by 0.61%–7.67%. Nevertheless, this strategy is unable to reduce or even increases the temperature difference in the absorber, which may induce larger thermal stress.

In this study, combining the advantages of FPTR with PTR-IT and overcoming their respective weaknesses, a novel finned PTR with inner tube (FPTR-IT, see Figure 1(d)) will be designed for solar cascade heat collection. Two HTFs will be employed to simultaneously provide heat sources with high and low temperatures for different applications, including power generation and domestic heating or desalination, etc. The inner tube, which is tightly attached to the upper part of the absorber, can present the high temperature HTF contacting the low heat flux region that illuminated by direct irradiance. Moreover, the heat from direct irradiance can be carried off by the low temperature HTF. As a result, the temperature at the directly illumined zone is expected to be effectively diminished, which contributes to preventing the occurrence of negative thermal-flux region. At the same
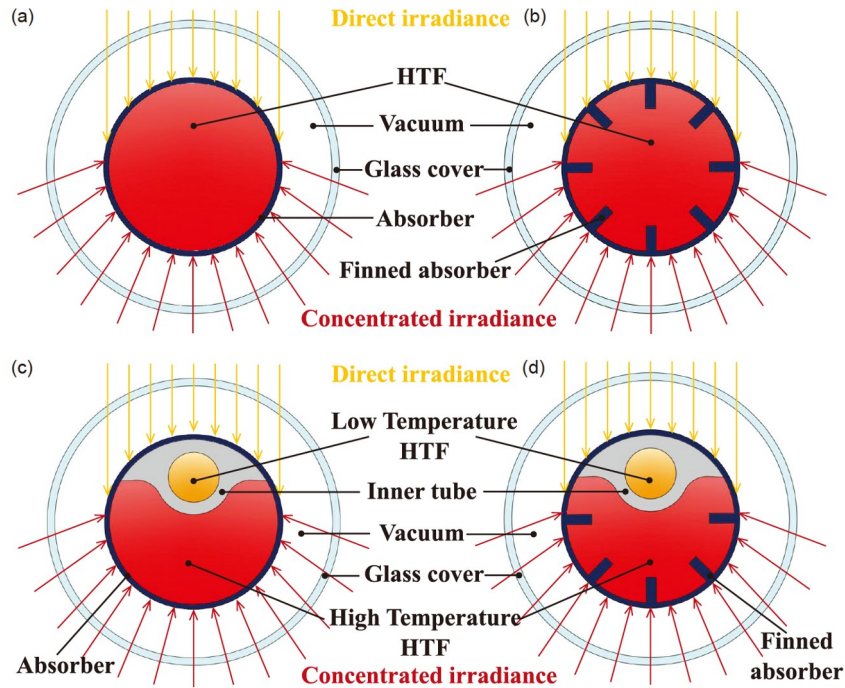
Figure 1 (Color online) Sketch of different PTRs and the novel FPTR-IT. (a) CPTR; (b) FPTR; (c) PTR-IT; (d) FPTR-IT.

time, the straight fins inside the lower part of the absorber will be employed and expected to decline the temperature in this region so as to dwindle the circumferential temperature difference. Based on design plan, numerical model will be developed to investigate performances of novel FPTR-IT. Then, the performance comparisons with CPTR, FPTR and PTR-IT will be conducted. Finally, the performance of FPTR-IT under broad ranges of oil flow rates, oil inlet temperatures and DNIs will be evaluated. This work may provide an alternative idea for designing highly efficient PTR for solar thermal cascade development and comprehensive utilization.

2   Model description

2.1   Physical model

The novel FPTR-IT in the present work is a modification from standard LS2 PTC [59], which may be manufactured by replacing the smooth absorber with a finned one and inserting an inner tube. The detailed geometric model and parameters of the FPTR-IT are presented and listed in Figure 2(a) and Table 1, respectively. The glass cover, absorber and inner tube are respectively made of Pyrex [30], stainless steel (321H) [59], and zirconia ceramic [60], whose properties are listed in Table 2. Water [61] and Syltherm-800 oil [62] are employed as the low and high temperature HTFs, respectively. Their temperature-dependent thermal properties are listed in Table 3. Moreover, concurrent flow is adopted for the two HTFs.

To determine the superiority of the novel FPTR-IT, three different types of PTRs (i.e., conventional PTR (CPTR), finned PTR (FPTR) and PTR with inner tube (PTR-IT)) are employed for comparative analysis (see Figure 1(a)–(c)). Moreover, their geometric parameters are set to be consistent with the novel FPTR-IT. It should be noted that for the FPTR, 8 straight fins are evenly arranged on inside of absorber tube circumferentially, while for the FPTR-IT, the 3 straight fins on the upper part of the absorber are removed due to the arrangement of the inner tube. Moreover, for the FPTR-IT and PTR-IT, both water and Syltherm-800 oil are applied to collecting heat with low and high temperature for domestic heating or desalination and power generation, while for the PTR and FPTR, only Syltherm-800 oil is adopted to produce heat source with high temperature for power generation. Performance of the PTRs at wide ranges of operating conditions, including different inlet temperatures ($T_{in,oil}$ = 400–600 K) and FRs (V_{oil} = 50–250 L/min) of Syltherm-800 oil as well as different DNIs (DNI = 300–1000 W/m^2), is comprehensively compared when inlet temperature ($T_{in,water}$) and FR (V_{water}) of water are set to 298.15 K and 3.6 L/min, respectively. In addition, to determine the effects of inlet temperature and FR of water, the performance of FPTR-IT under different $T_{in,water}$ (298.15–318.15 K) and V_{water} (3.6–10.8 L/min) when $T_{in,oil}$ = 500 K, V_{oil} = 50 L/min and DNI=1000 W/m^2 is investigated.

2.2   Boundary conditions and numerical methods

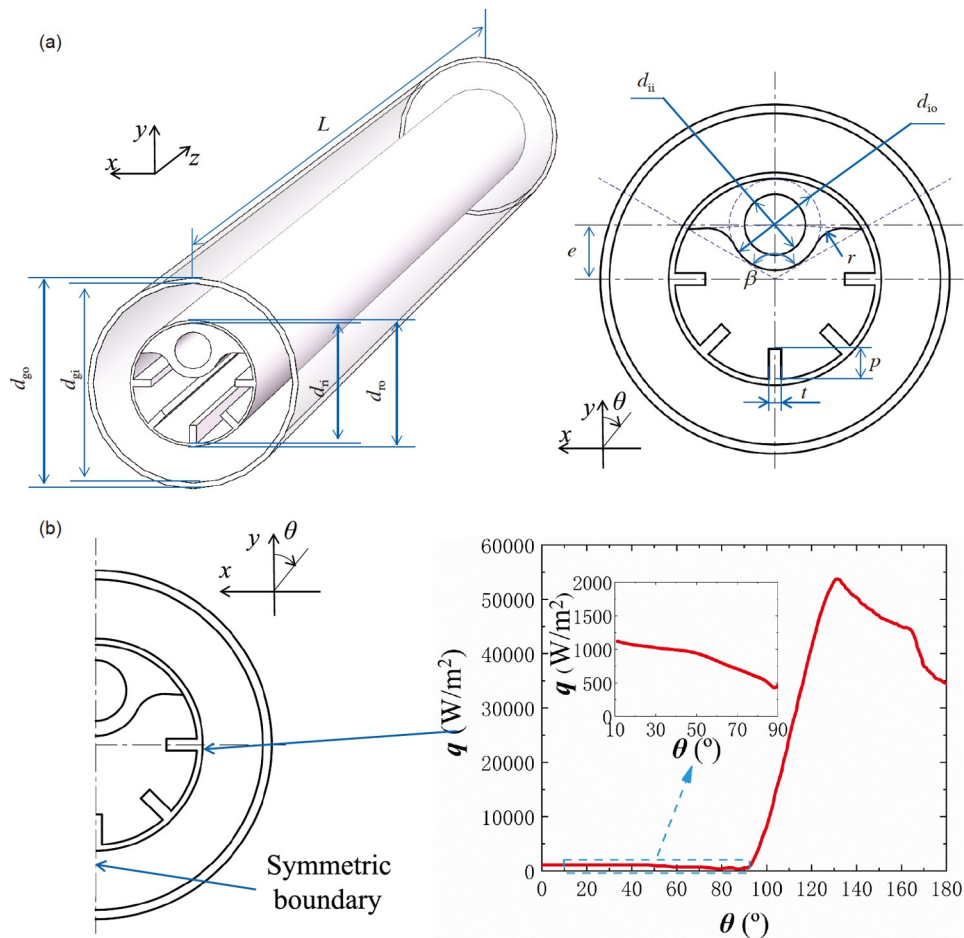Since the symmetry of the PTRs on the *y-z* plane, only half of

Figure 2 (Color online) Geometric model, computational domain of the FPTR-IT and the non-uniform heat flux [63]. (a) Geometric model; (b) computational domain and the non-uniform heat flux.

Table 1   Geometric parameters of the FPTR-IT

Parameter	Value	Parameter	Value
Length of PTR (L)	7.8 m	Outer diameter of glass cover (d_{go})	0.115 m
Inner diameter of glass cover (d_{gi})	0.109 m	Outer diameter of absorber (d_{ro})	0.07 m
Inner diameter of absorber (d_{ri})	0.066 m	Outer diameter of inner tube (d_{oi})	0.03 m
Inner diameter of inner tube (d_{ii})	0.02 m	Eccentric distance of inner tube (e)	0.018 m
Central angle (β)	120°	Radius of rounded corners (r)	0.01 m
Thickness of fin (t)	0.004 m	Height of the fin (p)	0.01 m

Table 2   Materials and thermal properties of solid domain

Domain	Material	λ (W/(m K))	ρ (kg/m³)	c_p (J/(kg K))
Absorber tube	Stainless steel [59]	25	7650	460
Glass cover	Pyrex [30]	1.2	2230	900
Inner tube	Zirconia ceramic [60]	0.4	5700	500

the FPTR-IT (see Figure 2(b) [63]) is applied in numerical simulation with symmetric boundary for saving computing resource. The detailed boundary conditions for the FPTR-IT from outside to inside are set as follows.

(1) Glass cover outer surface: A mixed boundary is

adopted to determine the heat exchanged from glass cover to environment or sky through convection and radiation. Gray body with emissivity of 0.86 is applied for glass cover [30]. A uniform heat transfer coefficient under a certain wind speed (V_w= 2.5 m/s) is defined [64]:

Table 3 Temperature-dependent thermal properties of HTFs

High temperature HTF (Syltherm-800 oil [62])	
Property	Equation
ρ (kg/m^3)	$-6.0616 \times 10^{-4}T^2 - 4.1535 \times 10^{-1}T + 1.1057 \times 10^3$
μ (Pa s)	$6.6720 \times 10^{-13}T^4 - 1.5660 \times 10^{-9}T^3 + 1.3882 \times 10^{-6}T^2 - 5.5412 \times 10^{-4}T + 8.4866 \times 10^{-2}$
λ (W/(m K))	$-5.7534 \times 10^{-10}T^2 - 1.8752 \times 10^{-4}T + 1.9002 \times 10^{-1}$
c_p (J/(kg K))	$1.7080T + 1.1078 \times 10^3$
Low temperature HTF (Water [61])	
Property	Equation
ρ (kg/m^3)	$1.772 \times 10^{-5}T^3 - 2.067 \times 10^{-2}T^2 + 7.335T + 1.71956 \times 10^2$
μ (Pa s)	$4.078 \times 10^{-11}T^4 - 5.502 \times 10^{-8}T^3 + 2.789 \times 10^{-5}T^2 - 6.302 \times 10^{-3}T + 0.536574$
λ (W/(m K))	$3.419 \times 10^{-8}T^3 - 4.581 \times 10^{-5}T^2 + 2.014 \times 10^{-2}T - 2.229$
c_p (J/(kg K))	$1.471 \times 10^{-6}T^4 - 1.973 \times 10^{-3}T^3 + 1.005T^2 - 2.2965 \times 10^2T + 2.3978 \times 10^4$

$$h_w = 4V_w^{0.58}d_{\text{go}}^{-0.42}. \tag{1}$$

Eq. (1) is applied on glass cover outer surface. In this study, the temperatures of ambient and sky are 298 and 290 K, respectively [65].

(2) Glass cover inner surface: Coupled thermal boundary is adopted to this surface.

(3) Absorber outer surface: The standard LS2 with optical efficiency of about 74.1% is applied in this work. By applying user defined function (UDF), the circumferential non-uniform heat flux (see Figure 2(b)) according to He's research [63] is applied on outer surface of absorber. For the standard LS2 PTC, the absorber outer surface is generally covered with cermet coating, which is beneficial to improve the absorption rate of solar irradiance and reduce the external thermal radiation loss. Furthermore, the selective coating has a temperature-dependent emissivity [66], which is described in eq. (2), is also considered herein.

$$\xi = 0.000327T - 0.065971. \tag{2}$$

(4) Interfaces between the HTFs and solid: No slip surface with coupled thermal boundary is adopted on inner surface of inner tube and absorber.

(5) End of the FPTR-IT: The ends of the glass cover, vacuum zone, absorber and inner tube are set to be adiabatic. At the inlets of the absorber and inner tube, velocity inlet condition is employed. The pressure outlet boundary condition is applied to the outlets of the absorber and inner tube.

In this numerical model, heat conduction in solid domains (glass cover, absorber and inner tube) and vacuum zone, heat radiation between glass cover and absorber and convective heat transfer of HTFs are all taken into consideration. For heat conduction in solid domain, the governing equation of energy is defined as follows:

$$\frac{\partial}{\partial x_i}\left(\lambda \frac{\partial T}{\partial x_i}\right) = 0, \tag{3}$$

where λ is thermal conductivity.

Discrete ordinates radiation model is employed to capture radiative heat transfer process between glass cover and absorber. Reynolds numbers for both high and low temperature HTFs corresponding to the flow-rate range are larger than 10000 in this study, and thus the flow of HTFs is in turbulent regime. To capture fluid flow and heat transfer process of HTFs, the realizable k-ε turbulence model is employed due to its advantages of predicting the flow features such as streamline curvature [67]. Governing equations for momentum, continuity, energy, turbulent energy dissipation (ε) and turbulent kinetic energy (k) are defined as below:

$$\frac{\partial(\rho u_i u_j)}{\partial x_i} = -\frac{\partial P}{\partial x_i} + \frac{\partial}{\partial x_j}\left((\mu + \mu_t)\left(\frac{\partial u_i}{\partial x_j} + \frac{\partial u_j}{\partial x_i}\right)\right.$$
$$\left. -\frac{2}{3}(\mu + \mu_t)\frac{\partial u_i}{\partial x_i}\delta_{ij} - \rho\overline{u'_i u'_j}\right), \tag{4}$$

$$\frac{\partial(\rho u_i)}{\partial x_i} = 0, \tag{5}$$

$$\frac{\partial(\rho u_i T)}{\partial x_i} = \frac{\partial}{\partial x_i}\left(\frac{\mu}{Pr} + \frac{\mu_t}{Pr_t}\right)\frac{\partial T}{\partial x_i}, \tag{6}$$

$$\frac{\partial(\rho u_i k)}{\partial x_i} = \frac{\partial}{\partial x_i}\left(\left(\mu + \frac{\mu_t}{\sigma_k}\right)\frac{\partial k}{\partial x_i}\right) + \Gamma - \rho\varepsilon, \tag{7}$$

$$\frac{\partial(\rho u_i \varepsilon)}{\partial x_i} = \frac{\partial}{\partial x_i}\left(\left(\mu + \frac{\mu_t}{\sigma_\varepsilon}\right)\frac{\partial \varepsilon}{\partial x_i}\right) + c_1\Gamma\varepsilon - \rho c_2\frac{\varepsilon^2}{k + \sqrt{v\varepsilon}}, \tag{8}$$

$$\Gamma = -\overline{u_i u_j}\frac{\partial u_i}{\partial x_i} = \mu_t\left(\frac{\partial u_i}{\partial x_j} + \frac{\partial u_j}{\partial x_i}\right)\frac{\partial u_i}{\partial x_i}, \tag{9}$$

where μ, ρ, μ_t and Pr are the viscosity, density, turbulent viscosity and Prandtl number of HTFs; Pr_t, σ_ε and σ_k represent turbulent Prandtl numbers for energy, ε and k, which are set to 0.85, 1.2 and 1.0, respectively.

The governing equations are solved through software ANSYS Fluent 16.0, and convective term is discretized by

employing the second order upwind scheme. For coupling pressure and velocity, SIMPLE algorithm is applied.

2.3 Parameter definitions

The parameters to evaluate performance of the PTR are expressed as below. The heat gain and PPC of water and Syltherm-800 oil are calculated as follows:

$$Q_{u,\text{water}} = \rho_{\text{water}} \cdot V_{\text{water}} \cdot c_{p,\text{water}} \cdot (T_{\text{out,water}} - T_{\text{in,water}}), \tag{10}$$

$$Q_{u,\text{oil}} = \rho_{\text{oil}} \cdot V_{\text{oil}} \cdot c_{p,\text{oil}} \cdot (T_{\text{out,oil}} - T_{\text{in,oil}}), \tag{11}$$

$$W_{p,\text{water}} = V_{\text{water}} \cdot \Delta P_{\text{water}}, \tag{12}$$

$$W_{p,\text{oil}} = V_{\text{oil}} \cdot \Delta P_{\text{oil}}, \tag{13}$$

where V_{water} and V_{oil} represent the FRs of water and Syltherm-800 oil, respectively. Based on eqs. (10)–(13), the total heat gain and PPC are defined as

$$Q_u = Q_{u,\text{oil}} + Q_{u,\text{water}}, \tag{14}$$

$$W_p = W_{p,\text{oil}} + W_{p,\text{water}}. \tag{15}$$

Thus, the total efficiency can be defined as follows:

$$\eta_{\text{total}} = \frac{Q_u - W_p / \eta_{\text{el}}}{A_a \cdot \text{DNI}}, \tag{16}$$

where η_{el} presents average electrical efficiency of thermal power station and is set to 0.33 according to ref. [19], and A_a is aperture area of PTC, and is 5 m × 7.8 m for LS2.

The parameters corresponding to fluid flow and heat transfer performance, including velocity of HTFs, Nusselt number (Nu), heat transfer coefficient (h), friction factor (f), Reynolds number (Re) and performance evaluation criteria (PEC) [68], are calculated as follows:

$$u = \frac{4V}{\pi d^2}, \tag{17}$$

$$Nu = hd / \lambda, \tag{18}$$

$$h = q_w / (T_w - T_m), \tag{19}$$

$$f = \frac{2\Delta Pd}{\rho u^2 L}, \tag{20}$$

$$Re = \frac{\rho u d}{\mu}, \tag{21}$$

$$\text{PEC} = \frac{Nu / Nu_0}{(f / f_0)^{1/3}}, \tag{22}$$

where V, μ, ρ and λ are the FRs, viscosity, density and thermal conductivity of HTFs at average temperature (T_m), d represents the inner diameter of absorber (d_{ri}) for the Syltherm-800 oil and inner diameter of the inner (d_{ii}) tube for water, T_w and q_w respectively represent average wall temperature and heat flux on the interface between the HTFs and solid zones, and ΔP represents the pressure drop between the inlet and outlet. Nu_0 and f_0 represent the Nusselt number and friction factor of the smooth tube, respectively. The tem-

perature difference of absorber, which represents temperature uniformity of absorber, is defined as

$$\Delta T = T_{\text{max}} - T_{\text{min}}, \tag{23}$$

where T_{max} and T_{min} are the maximum and minimum temperatures in the absorber, respectively.

3 Grid system and model verification

3.1 Grid independence test

A grid system of FPTR-IT with hexahedral mesh is generated through software Gambit, as displayed in Figure 3. The mesh of fluid domain at the region near the interface is sufficiently refined to ensure the y^+ less than 1 and capture the flow and heat transfer characteristics in boundary layer. In addition, a grid independence test is conducted through four different grid systems with mesh numbers of 314678, 632424, 1015404, and 2764320 when $V_{\text{oil}} = 50$ L/min, $T_{\text{in,oil}} = 500$ K and DNI = 1000 W/m^2. It is found that the relative deviations of η_{total}, Nu_{oil}, f_{oil}, T_{max} and ΔT are less than 0.1% as the mesh number raises from 1015404 to 2764320. Thus, the grid system with 1015404 meshes can obtain sufficient accuracy with relatively few resources, which is selected for the following numerical simulation.

3.2 Numerical model verification

Friction factor (f) and Nusselt number (Nu) of CPTR obtained from numerical simulation are validated through Petukhov's correlation and Gnielinski correlation [69]:

$$f = (0.790\ln Re - 1.64)^{-2}, \tag{24}$$

$$Nu = \frac{(f / 8)(Re - 1000)Pr}{1 + 12.7(f / 8)^{0.5}(Pr^{2/3} - 1)}\left[1 + \left(\frac{d}{L}\right)^{2/3}\right]. \tag{25}$$

The relative deviation between the numerical results and correlations or experimental data is calculated as

$$\delta = (A - A_0) / A_0 \times 100\%, \tag{26}$$

where A is the numerical result, while A_0 is the correlation values or experimental data.

The results from the numerical simulation and correlations for oil flow in CPTR are presented in Figure 4(a). Relative deviations of f and Nu under the range of conditions studied in this work are limited in ±5.5% and ±13.4%, respectively. The comparisons of f and Nu between numerical results and correlations for water flow in inner tube are displayed in Figure 4(b). The results indicate that the numerical results agree well with the correlations and the relative deviations of f and Nu are limited in ±8.1% and ±19.8%, respectively. Moreover, comparisons between experimental data and numerical results at operating conditions (see Table 4) from Dudley's research [70] are conducted to further verify model
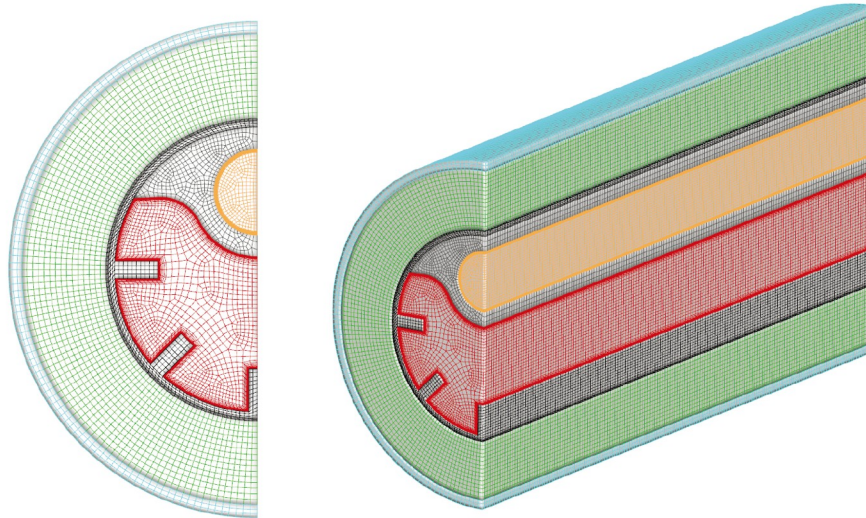
Figure 3   (Color online) Grid system of FPTR-IT.
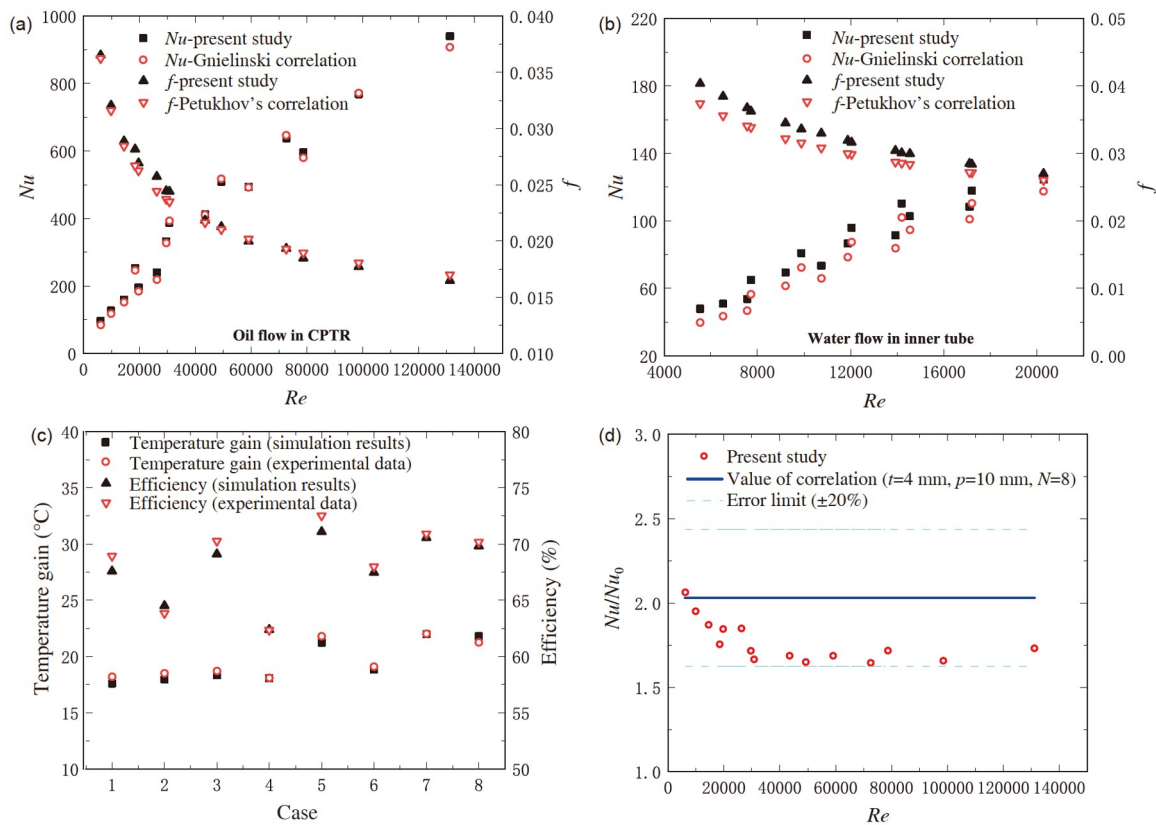

Figure 4   (Color online) Results of model validations. (a) Validation for oil in CPTR; (b) validation for water in inner tube; (c) comparison with experimental data for CPTR; (d) comparison with correlation for FPTR.

reliability. The results in Figure 4(c) indicate that the developed model agrees well with experimental data, and relative deviations of efficiency and temperature are limited within ±1.9% and ±3.3%, respectively. Therefore, the numerical model established herein is accurate enough for capturing heat transfer processes in PTRs.

In addition, correlation of Nusselt number ratio (Nu/Nu_0) for finned tube [57]

Table 4 Operating conditions of Dudley's research [70]

	Case							
	1	2	3	4	5	6	7	8
DNI (W/m^2)	880.6	903.2	909.5	920.9	933.7	937.9	968.2	982.3
FR (L/min)	55.60	56.30	54.70	56.80	47.70	55.50	47.78	49.10
$T_{in,oil}$ (K)	572.15	629.05	523.85	652.65	375.35	570.95	424.15	470.65
Wind speed (m/s)	2.9	4.2	3.3	2.6	2.6	1.0	3.7	2.5
Air temperature (K)	300.65	304.25	299.35	302.65	294.35	301.95	295.55	297.45

$$Nu / Nu_0 = \left(\frac{L_c}{d_{ri}}\right)^{-0.5} \cdot \left(\frac{A_0}{A_{real}}\right)^{0.8} \cdot \left(\frac{PER_{real}}{PER_0}\right)^{0.29} \quad (27)$$

is employed to validate model reliability for simulating FPTR, where the ratio of characteristic length (L_c) and absorber diameter can be calculated as below:

$$\frac{L_c}{d_{ri}} = \left(\frac{A_{core}}{A_{real}}\right) \cdot \left(1 - 2\frac{p}{d_{ri}}\right)$$
$$+ \left(\frac{A_{fin}}{A_{real}}\right) \cdot \left[\left(\frac{\pi}{N}\right) \cdot \left(1 - 2\frac{p}{d_{ri}}\right) - \frac{t}{d_{ri}}\right], \quad (28)$$

where N is the number of fins, A_0, A_{fin}, A_{real}, and A_{core} are sectional areas of smooth absorber and fins, fluid in finned absorber, and core tube area, respectively:

$$A_0 = \pi \cdot d_{ri}^2 / 4, \quad (29)$$

$$A_{fin} = N \cdot p \cdot t, \quad (30)$$

$$A_{core} = \pi \cdot (d_{ri} - 2 \cdot p)^2 / 4, \quad (31)$$

$$A_{real} = A_0 - A_{fin}. \quad (32)$$

PER_0 and PER_{real} are the wet perimeters of the smooth and finned absorbers, respectively:

$$PER_0 = \pi \cdot d_{ri}, \quad (33)$$

$$PER_{real} = PER_0 + 2 \cdot N \cdot p. \quad (34)$$

Figure 4(d) displays the Nu/Nu_0 obtained from numerical simulation and calculated from correlation. It is observed that the numerical results are slightly smaller than the value of correlation with the relative deviation being less than 20%. The numerical model has sufficient accuracy in this study.

4 Results and discussion

4.1 Comparisons of velocity, temperature and heat flux distribution

Velocity and temperature distributions are the key parameters that affect the heat transfer process and its performance in PTRs. Figure 5(a) and (b) present the velocity and temperature distributions on cross-section planes ($z = 3.9$ m) of different PTRs when $T_{in,oil} = 500$ K, $V_{oil} = 50$ L/min and

DNI= 1000 W/m^2. From CPTR to FPTR-IT, the oil velocity magnifies when operating at the same FR due to increase of its cross-sectional area, as depicted in Figure 5(a). While the velocity contours of the water of PTR-IT and FPTR-IT are almost the same at a constant FR. In addition, compared with CPTR, the velocity gradients of oil near the surfaces of absorber or fins in enhanced PTRs are apparently magnified, especially the FPTR-IT obtains the largest velocity gradient. This will contribute to augmenting convective heat transfer between oil and absorber. Therefore, the temperatures of absorbers (especially at the lower part) in enhanced PTRs are dramatically reduced, as shown in Figure 5(b).

For FPTR, the straight fins can expand the heat transfer area between oil and absorber and thus bring down the absorber temperature. For PTR-IT, the low heat flux from direct irradiance on the upper part of absorber can be quickly carried off by the water with low temperature. Therefore, the temperature on the upper part of absorber is dramatically diminished to even lower than the oil temperature. As expected, the FPTR-IT combines the advantages of FPTR and PTR-IT and obtains the lowest temperature of absorber, which is beneficial to cut down the heat loss and enhance the total efficiency.

To quantitatively compare the temperature and heat loss among different PTRs, the temperatures and outward heat flux along circumferential direction on outer surfaces of absorber in different PTRs are displayed in Figure 5(c) and (d) for discussion. As shown in Figure 5(c), it is viewed that compared with the CPTR, all the three different enhanced PTRs can minify the temperature on outer surfaces of the absorber at the whole circumference. In addition, for the FPTR, the temperature on the lower half part of absorber outer surface ($90° < \theta < 180°$), where is loaded with extremely high heat flux, is significantly reduced by about 50 K. While the temperature on the upper part of absorber outer surface ($0° < \theta < 90°$) is close to $T_{in,oil}$ (500 K) and its reduction is not obvious. It is because this area is only loaded with much lower heat flux from direct irradiance. For the PTR-IT, on the lower half part of absorber ($90° < \theta < 180°$), the circumferential temperature distribution on absorber outer surface is similar to that of FPTR. It is because the insertion of the inner tube magnifies the oil velocity (see Figure 5(a)) and thus enhances the convective heat transfer at lower half part of
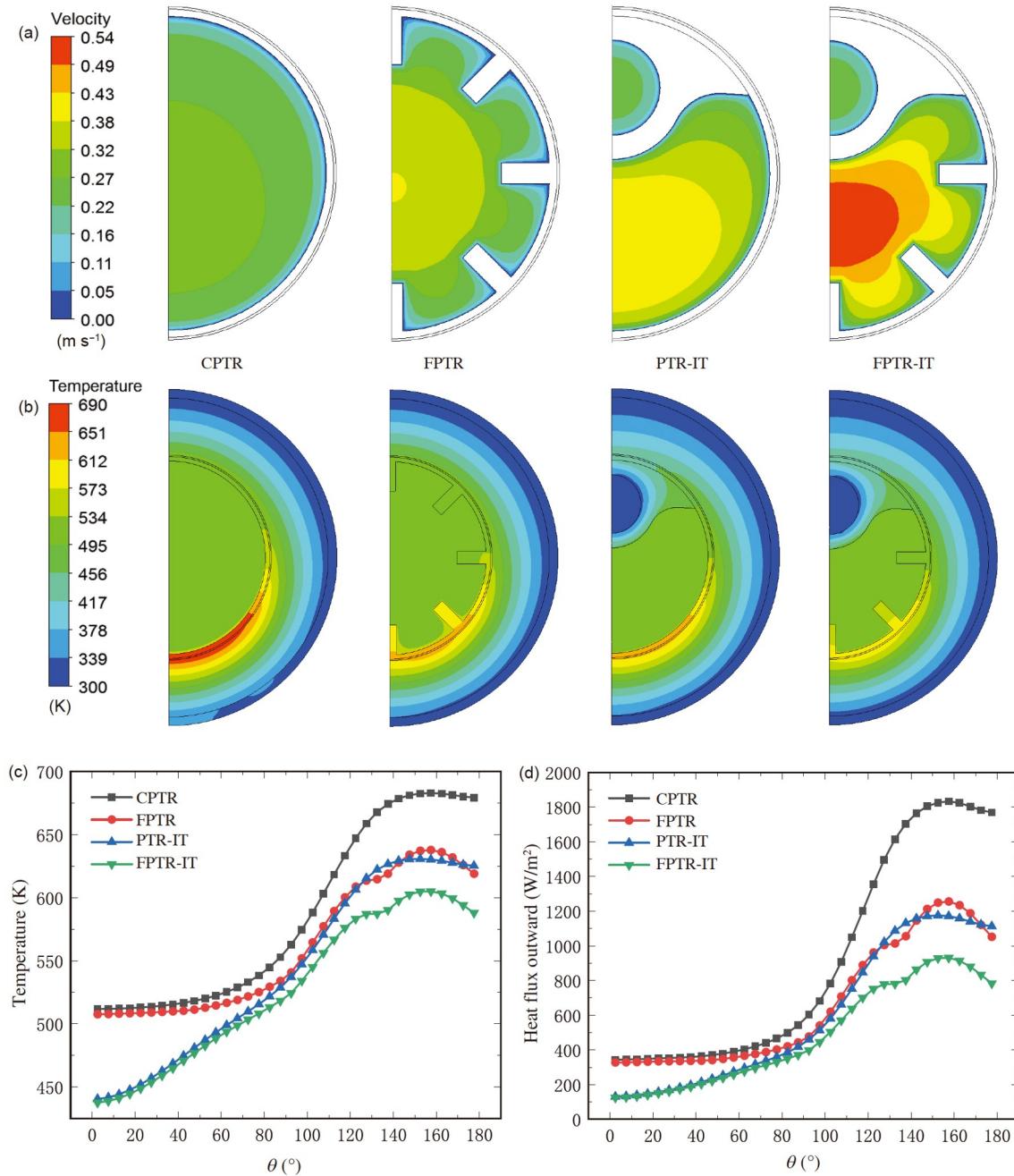
Figure 5   (Color online) Velocity, temperature and outward heat flux distributions of the PTRs when $T_{in,oil}$ = 500 K, V_{oil} = 50 L/min and DNI= 1000 W/m^2. (a) Velocity; (b) temperature; (c) circumferential distribution of temperature; (d) circumferential distribution of outward heat flux.

absorber. Especially, on upper part of absorber (0°<θ<90°), due to the low heat flux from direct irradiance in this area being carried away quickly by the low temperature HTF (water), the temperature of absorber is dramatically diminished (up to about 75 K) when compared with the CPTR. For the FPTR-IT, temperature on lower half part of absorber outer surface is further visibly reduced when compared with PTR-IT due to the heat transfer being further enhanced by the straight fins. Moreover, the temperature on upper part of absorber outer surface for FPTR-IT is similar to that of PTR-

IT with a slight decrease. Therefore, the FPTR-IT achieves the lowest temperature of the absorber as expected. From Figure 5(d), it is observed that when compared with CPTR, the outward heat fluxes on outer surfaces of absorber in enhanced PTRs are also apparently reduced. Moreover, the circumferential outward heat fluxes perform the similar trends as the temperatures in Figure 5(c). It is because the radiation heat transfer flux between glass cover and absorber accounts for major part of outward heat flux, which is dominated by outer surface temperature of absorber.

4.2 Performance comparisons under different operating conditions

To determine performances and superiority of FPTR-IT proposed herein, comparisons of performances among the FPTR-IT and other PTRs under different operation conditions, including V_{oil}, $T_{in,oil}$ and DNI, are performed and discussed in details below.

4.2.1 Comparisons under different oil flow rates

The performance of FPTR-IT and other PTRs under a typical range of oil flow rates (50–250 L/min) when $T_{in,oil} = 500$ K and DNI = 1000 W/m^2 is compared. Figure 6(a) and (b) present the maximum temperatures and temperature differences of the absorber in different PTRs. It is viewed that the maximum temperature and temperature difference of every PTR decrease with increasing V_{oil}. The reason is that as V_{oil} increases, convective heat transfer rate of oil is enhanced and

thus heat from solar irradiance can be carried off faster. Hence, the temperature and its gradient in absorber will shrink with rising V_{oil}. Moreover, compared with the CPTR, it is found that the three enhanced PTRs can obviously decline the maximum temperature at all FRs and the reduction amplitudes of maximum temperature all decline with the increase of the V_{oil}, as shown in Figure 6(a). Among three enhanced PTRs, the FPTR-IT proposed in this work obtains the lowest maximum temperature. It needs to be noted that the temperature differences of absorbers in PTR-IT and FPTR-IT are higher than that of CPTR at relative high V_{oil} (V_{oil}>100 L/min). It is because the temperature at the upper part of the absorber is decreased more than that of lower part due to the inner tube, which can be viewed intuitively from Figure 5(c).

The Reynolds (*Re*) numbers corresponding to the oil FRs when $T_{in,oil} = 500$ K are located at the range of 14517 to
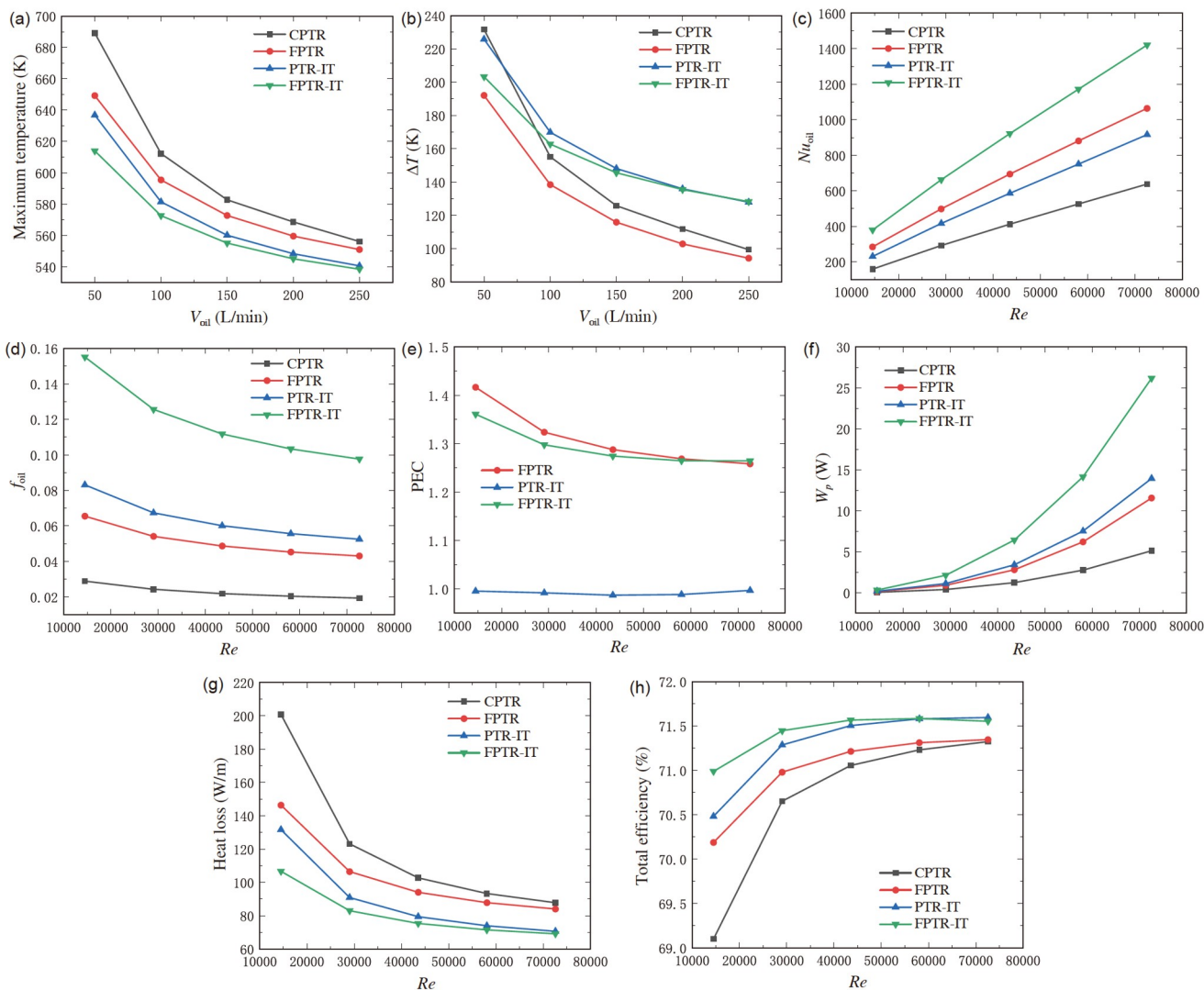

Figure 6 (Color online) Performances of different PTRs with rising V_{oil} or *Re*. (a) Maximum temperature; (b) temperature difference; (c) Nusselt number for oil flow; (d) fraction factor for oil flow; (e) PEC for oil flow; (f) PPC; (g) heat loss; (h) total efficiency.

72585. Figure 6(c)–(h) show the Nusselt number (Nu_{oil}), friction factor (f_{oil}), PEC of oil, PPC (W_p), heat loss and total efficiency of the PTRs over Reynolds number. It is clear that both Nu_{oil} and W_p of each PTR increase with raising Re number. In addition, both f_{oil} and PEC decrease with the increase of Re, and the FPTR-IT obtains a moderate PEC (1.26–1.36), which is slightly lower than that of FPTR but much higher than that of PTR-IT. Most importantly, it is viewed that the FPTR-IT can dramatically augment the heat transfer of oil and obtains the highest Nu_{oil} at all Re numbers, which is 2.23 to 2.38 times that of the CPTR. As a result, the heat losses to environment of the PTRs decline with the increase of Re number due to the reduction of absorber temperature. Moreover, the FPTR-IT achieves the lowest heat loss at all Re numbers and the heat loss is dramatically reduced by 18.68–94.20 W/m (relative reduction in heat loss ranges in 21.3%–46.9%) when compared with the CPTR. As the heat losses are effectively reduced, the total efficiencies

of the enhanced PTRs are consequently improved and have the opposite trends as the heat losses, as displayed in Figure 6(h). In addition, the FPTR-IT obtains the highest total efficiency at almost all Re numbers, which is effectively improved by 0.23%–1.89% when comparing with the CPTR. It should be noted that when $Re>60000$, the total efficiency of FPTR-IT is lower than that of the PTR-IT, which is because the W_p of the FPTR-IT is much larger than that of the PTR-IT at a high V_{oil}.

4.2.2 Comparisons under different oil inlet temperatures

The comparisons of performance among FPTR-IT and other PTRs with different oil inlet temperatures when V_{oil} = 50 L/min and DNI = 1000 W/m^2 are discussed. The maximum temperatures and temperature differences of the absorber in different PTRs are respectively depicted in Figure 7(a) and (b). It is viewed from Figure 7(a) that maximum temperatures of all PTRs increase with rising $T_{in,oil}$. Under the
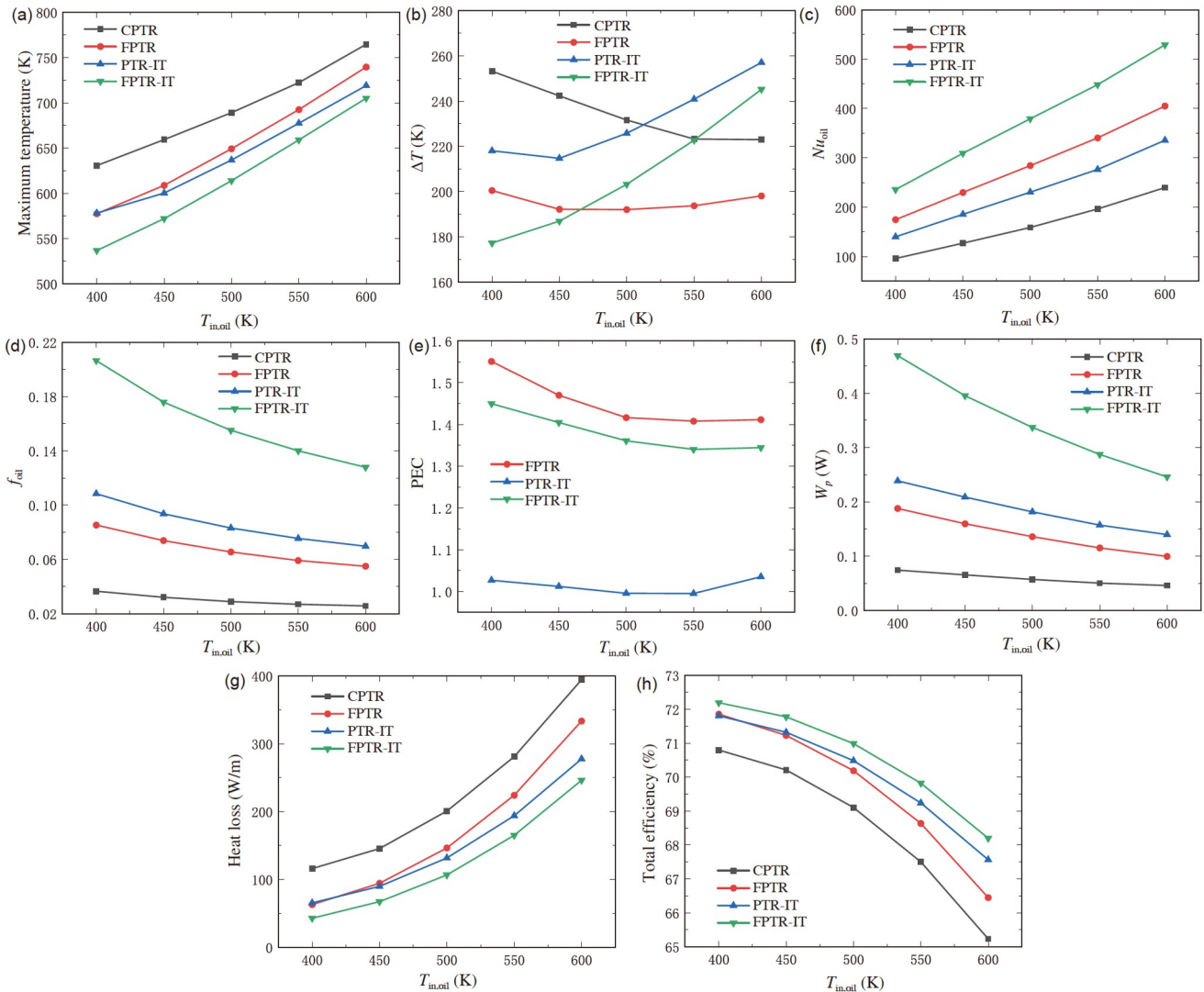

Figure 7 (Color online) Performances of different PTRs with raising $T_{in,oil}$. (a) Maximum temperature; (b) temperature difference; (c) Nusselt number for oil flow; (d) fraction factor for oil flow; (e) PEC for oil flow; (f) PPC; (g) heat loss; (h) total efficiency.

range of $T_{\text{in,oil}}$ studied herein, the maximum temperature of FPTR-IT is always the lowest. Furthermore, compared with the CPTR, the reduction in maximum temperature of the FPTR-IT declines gradually with the increase of $T_{\text{in,oil}}$, which is ranged in 59.5–93.9 K. The temperature differences of the four PTRs have different trends, as displayed in Figure 7(b). And for FPTR-IT and PTR-IT, the temperature differences rise with the increase of $T_{\text{in,oil}}$. It is because the temperature in the upper part of the absorber increases less with $T_{\text{in,oil}}$ due to the water with relative lower temperature (298.15 K) in the inner tube, while the temperature in the lower part of the absorber increases markedly with $T_{\text{in,oil}}$. For the FPTR and PTR, the temperature differences decrease first and then stabilize or increase slightly.

Figure 7(c)–(h) present variations of Nu_{oil}, f_{oil}, PEC, W_p, heat loss and total efficiency of PTRs with $T_{\text{in,oil}}$. With the increase of temperature, the viscosity of the oil will diminish according to Table 3. Therefore, the convective heat transfer will be enhanced while the flow resistance will be weakened with raising $T_{\text{in,oil}}$. As $T_{\text{in,oil}}$ increases, Nu_{oil} of all PTRs increase while f_{oil}, PEC and W_p of all PTRs decline, as shown in Figure 7(c)–(f). Moreover, the FPTR-IT achieves the highest Nu_{oil} and W_p at all $T_{\text{in,oil}}$, which are 2.21–2.45 and 3.88–5.12 times that of the CPTR. The PEC value of FPTR-IT is located in range of 1.34–1.45, which is slightly lower than that of FPTR but much higher than that of PTR-IT. From Figure 7(g) and (h), it can be found that the heat loss and total efficiency show opposite trends. As the $T_{\text{in,oil}}$ increases, the heat loss rises and the total efficiency decreases consequently. In addition, the FPTR-IT obtains the best performance with the heat loss being reduced by 73.2–148.1 W/m (37.6%–63.2%) and the total efficiency being improved by 1.39%–2.96%.

4.2.3 Comparisons under different DNIs

The performance evaluation of PTRs is with typical broad extents of DNI (300–1000 W/m²). Figure 8(a) and (b) depict
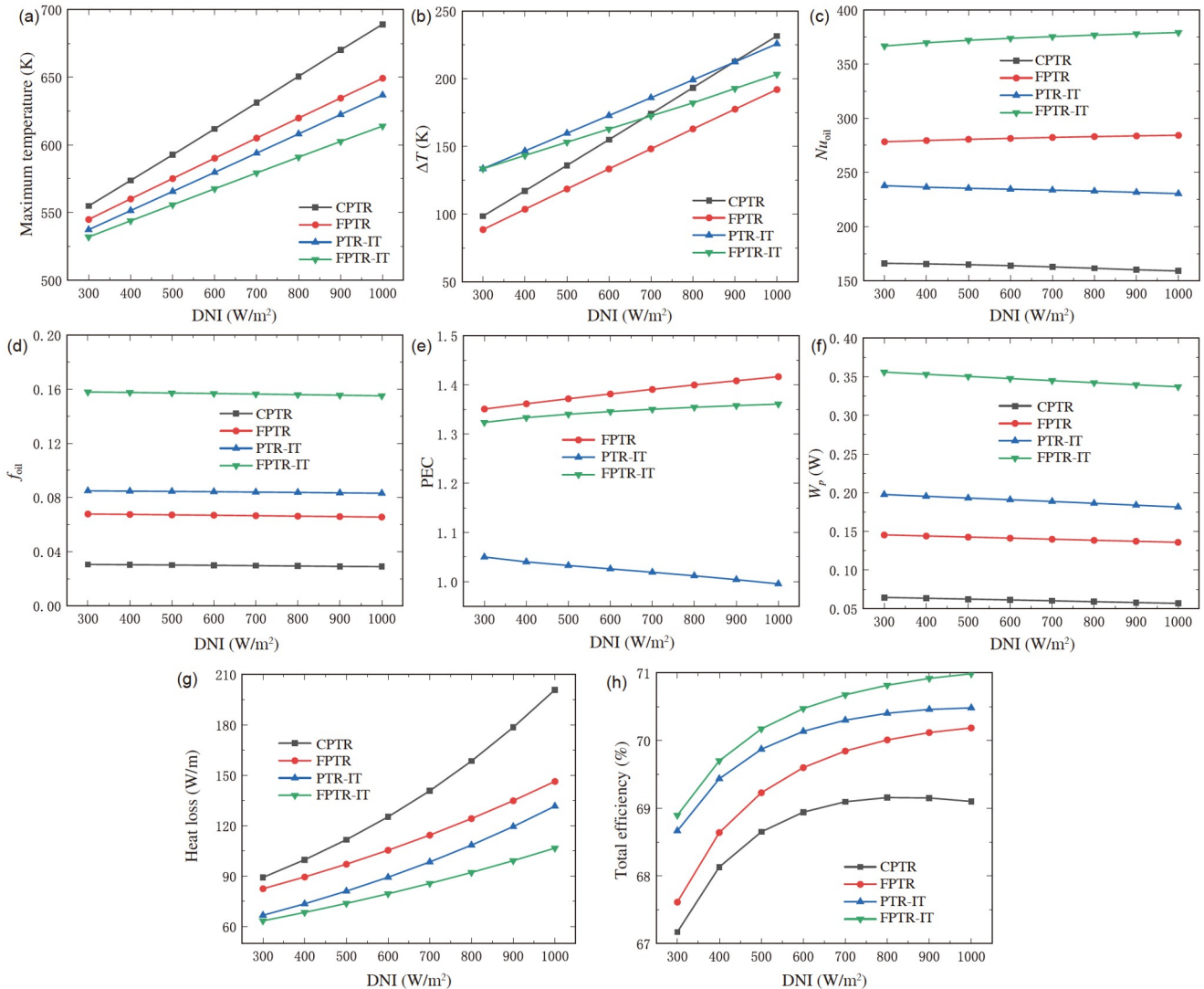

Figure 8 (Color online) Performances of different PTRs with rising DNI. (a) Maximum temperature; (b) temperature difference; (c) Nusselt number for oil flow; (d) fraction factor for oil flow; (e) PEC for oil flow; (f) PPC; (g) heat loss; (h) total efficiency.

variations of maximum temperatures and temperature differences of absorbers in PTRs with DNI when V_{oil} = 50 L/min and $T_{in,oil}$ = 500 K. It is observed both the maximum temperature and temperature difference for each PTR rise linearly with raising DNI. In addition, the FPTR-IT achieves the lowest maximum temperature at all DNIs considered herein. Compared with CPTR, the temperature differences of three enhanced PTRs increase more gently. Moreover, it is worth to note that the temperature differences of absorbers in FPTR-IT and PTR-IT are higher than that of CPTR at low DNI because the temperature reduction at the upper part of absorber is much larger than that at the lower part of absorber under a low DNI, as shown in Figure 8(b).

Variations of Nu_{oil}, f_{oil}, PEC, W_p, heat loss and total efficiency of different PTRs with increasing DNI are presented in Figure 8(c)–(h). It is clear that all the Nu_{oil}, f_{oil}, PEC and W_p for each PTR vary slightly with DNI. This is because the heat transfer and flow resistance are generally less affected by thermal boundaries but greatly influenced by flow regimes. Thus, the DNI only slightly affects the Nu_{oil}, f_{oil}, PEC and W_p through changing the properties of the oil. Furthermore, it is found that the FPTR-IT achieves the best heat transfer performance (largest Nu_{oil}) accompanied by the

highest f_{oil} and W_p. And the FPTR-IT obtains a moderate PEC value. With the increase of DNI, the heat flux into absorber raises and its temperature increases consequently. Thus, the heat losses of all PTRs increase with rising DNI, as shown in Figure 8(g). Moreover, heat loss of FPTR-IT is the lowest and its growth with DNI is the slowest among four PTRs. Although the heat loss of each PTR increases with rising DNI, the total efficiency still raises with the increase of DNI because the heat absorbed from solar irradiance increases more sharply than the heat loss. Especially, when DNI >800 W/m², the total efficiency of CPTR starts to slowly decline because the growth of the heat loss begins to overcome that of the heat gain. Most importantly, the FPTR-IT can always gain the highest total efficiency at all studied DNIs. Moreover, compared with the CPTR, the total efficiency of the FPTR-IT is effectively improved by 1.52%–1.89%.

4.3 Performance evaluation of FPTR-IT

4.3.1 Performance evaluation of FPTR-IT under different V_{oil}, $T_{in,oil}$ and DNI

Comprehensive evaluation of performance of FPTR-IT proposed herein is important for guiding its practical application. Figure 9(a) and (b) depict heat loss of FPTR-IT under
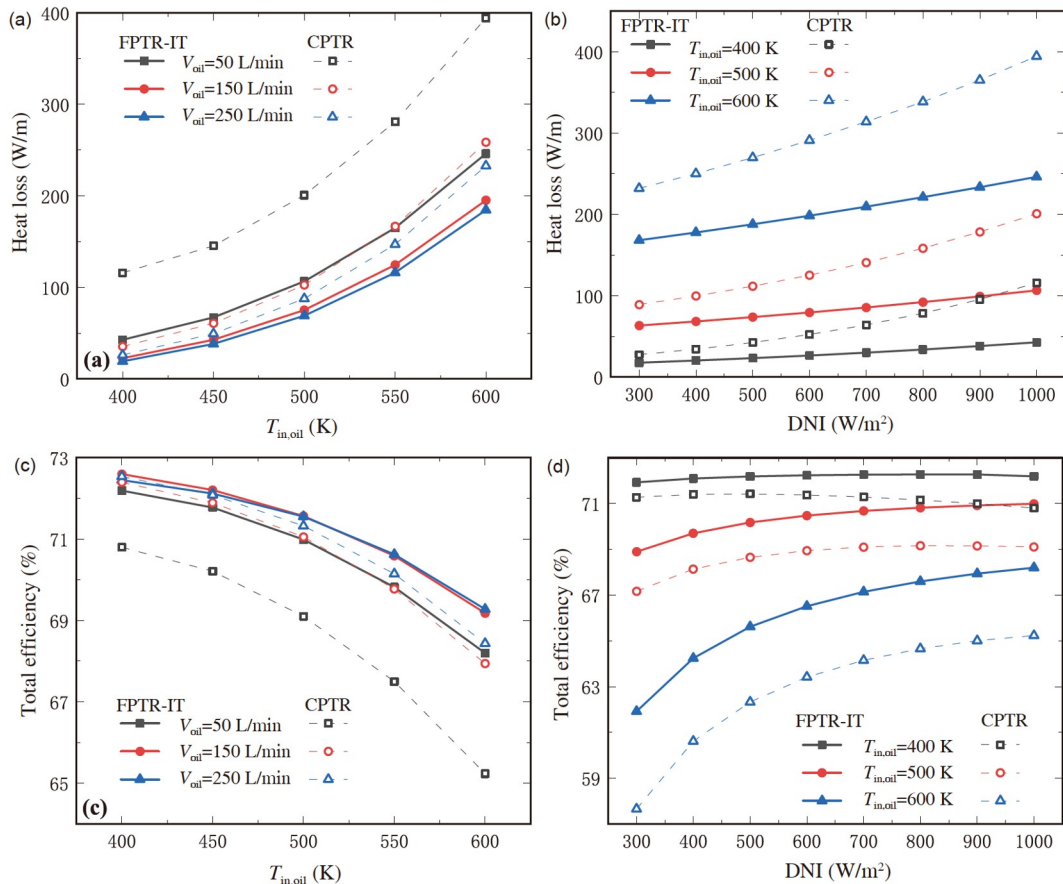

Figure 9 (Color online) Heat losses and total efficiencies of FPTR-IT and CPTR under broad ranges of V_{oil}, $T_{in,oil}$, and DNIs. (a) Heat loss under different V_{oil} and $T_{in,oil}$; (b) heat loss under different $T_{in,oil}$ and DNI; (c) total efficiency under different V_{oil} and $T_{in,oil}$; (d) total efficiency under different $T_{in,oil}$ and DNI.

broad ranges of operation conditions with the performance of CPTR as comparison. It is viewed that heat losses of both FPTR-IT and CPTR increase with raising $T_{in,oil}$ and DNI, but decrease with rising V_{oil}. Compared with CPTR, the heat loss of FPTR-IT is efficaciously reduced by 9.9–148.1 W/m (20.7%–63.2%) at all operation conditions studied herein. In addition, the reduction in heat loss raises with increasing $T_{in,oil}$ and DNI and declines with the increase of V_{oil}. Figure 9(c) and (d) present the total efficiencies of FPTR-IT and CPTR under broad ranges of V_{oil}, $T_{in,oil}$ and DNIs. Total efficiency of FPTR-IT increases with declining $T_{in,oil}$ and rising DNI. With V_{oil} increasing, the total efficiency of the FPTR-IT increases firstly and then begins to decline when V_{oil}>150 L/min and $T_{in,oil}$<500 K. Moreover, although total efficiency of FPTR-IT is slightly reduced when compared with CPTR at high V_{oil} (>150 L/min) and low $T_{in,oil}$ (<450 K) because of the large PPC, the FPTR-IT can improve the total efficiency by 0.03%–4.27% at all other studied conditions.

FPTR-IT can achieve solar cascade heat collection namely provide different grades of thermal energy. The apportionments of heat gains for low and high temperature HTFs (water and oil) are the key characteristics of the cascade heat collection system. The proportions of heat gains for water and oil in the total input solar energy at different operation conditions are depicted in Figure 10(a) and (b). It is viewed that both the proportions of water and oil heat gains vary little with V_{oil}. As $T_{in,oil}$ increases, more heat is transferred from oil to water due to raising temperature difference between oil and water, and thus the proportion of water heat gain rises accompanied with decrease of oil heat gain. The proportion of heat gain of water declines with the rising DNI, while that of oil performs the opposite trends, as shown in Figure 10(b). The reason for this phenomenon is that the heat absorbed by oil augments much more sharply than that of the water. Especially, when $T_{in,oil}$ ≥600 K and DNI <400 W/m^2, the proportion of oil heat gain is even negative due to the heat exchanged from oil to water outweighing the solar heat input. In addition, the proportions of heat gains for water and oil under the studied conditions herein are ranged in 8.3%–73.9% and −12.0%–64.3%, respectively. Figure 10(c) and (d) display the temperature gains of water and oil under broad ranges of V_{oil}, $T_{in,oil}$, and DNIs. It is observed that the temperature gain of water increases obviously with rising $T_{in,oil}$ and slightly with raising V_{oil} and DNI, while that of oil increases with raising DNI and decreases with rising V_{oil} and $T_{in,oil}$. Moreover, the temperature gains of water and oil under
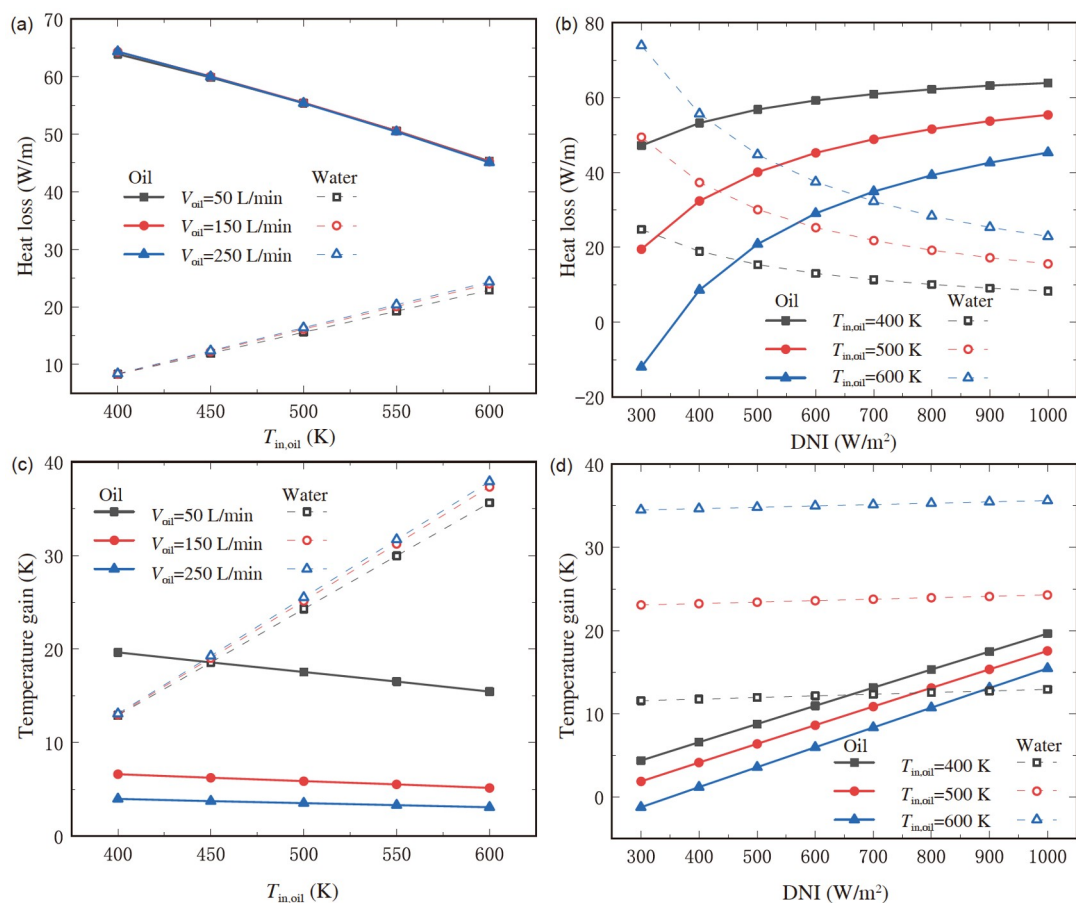

Figure 10   (Color online) Performances of cascade heat collection for FPTR-IT at broad ranges of V_{oil}, $T_{in,oil}$, and DNIs. (a) Heat gain under different V_{oil} and $T_{in,oil}$; (b) heat gain under different $T_{in,oil}$ and DNI; (c) temperature gain under different V_{oil} and $T_{in,oil}$; (d) temperature gain under different $T_{in,oil}$ and DNI.

the studied conditions herein are ranged in 11.6–37.9 K and −1.2–19.6 K, respectively.

4.3.2 Performance evaluation of FPTR-IT under different V_{water} and $T_{in,water}$

Figure 11 presents the influences of V_{water} and $T_{in,water}$ on the performance of FPTR-IT when $T_{in,oil}$ = 500 K, V_{oil} = 50 L/min and DNI= 1000 W/m². With the increasing V_{water} or decreasing $T_{in,water}$, the heat loss is reduced slightly and consequently the total efficiency of FPTR-IT is improved. In addition, the heat gain and temperature gain of oil decrease slightly with the increasing V_{water} or decreasing $T_{in,water}$, and the heat gain and temperature gain of water perform the opposite trends. In summary, V_{water} and $T_{in,water}$ have relative little effect on the performance of FPTR-IT except V_{water} has great influence on the temperature gain of water.

4.3.3 Comparisons with other research works

Table 5 [47,48,57,66,71–79] lists the performance comparisons such as maximum thermal efficiencies and their improvement between the present work and relevant published research work. The types of research methods, modifications of PTR and HTFs and operating conditions such as inlet temperature of HTF and DNI employed in the work are also

listed. It is observed that the numerical analysis method is employed in most studies including this work due to the difficulty and high cost of experiment. Kalidasan et al. [71–73] has conducted several creative experimental works to improve the performance of PTR. In addition, since the types of HTF and operating conditions vary from study to study, it is difficult to conduct a rigorous comparison between the present work and relevant published work. But compared with the work under the same HTF and similar operating conditions, the present work can obtain a moderate thermal efficiency and improvement in thermal efficiency. Thus, it can be concluded that the FPTR-IT has a promising potential in improving performance of PTR.

5 Conclusions

This paper designed a novel FPTR-IT with high efficiency for providing different grades of thermal sources. A numerical model was developed and validated for analyzing and evaluating performances of novel FPTR-IT. Moreover, comprehensive comparisons with other PTRs and performance evaluation under broad ranges of operating conditions were studied and discussed. The main conclusions can be
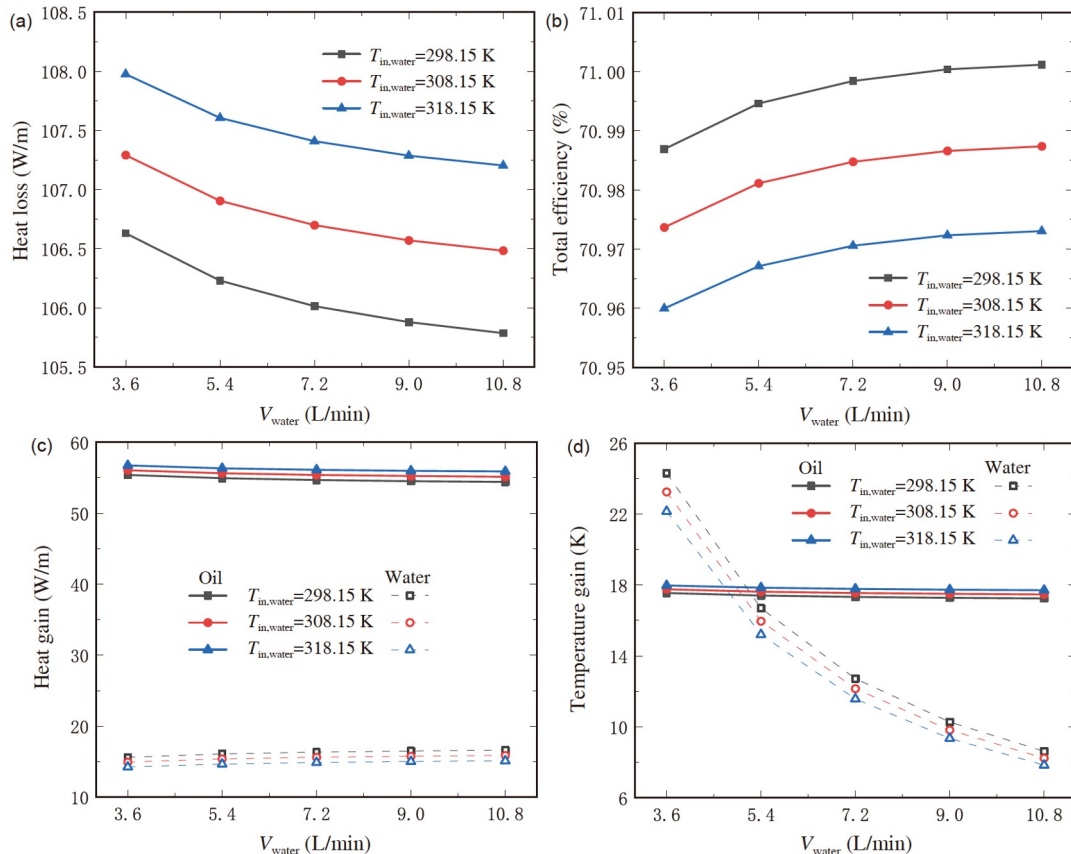

Figure 11 (Color online) Performances of cascade heat collection for FPTR-IT at different V_{water} and $T_{in,water}$. (a) Heat loss; (b) total efficiency; (c) heat gain; (d) temperature gain.

Table 5　Comparisons between other works and the present work

Reference	Study methods	Type of modifications	Type of HTFs	Inlet temperature of HTF (K)	DNI (W/m^2)	Maximum thermal efficiency (%)	Improvement in thermal efficiency (%)
Kalidasan et al. [71]	Experimental	Internal hinged blades	Water	314.25–349.75	592.72–818.52	70.82	8.51
Chakraborty et al. [74]	Numerical analysis	Helical coil-insert	Al$_2$O$_3$/ water and water	298–308	432–750	76.37	11.02
Muñoz et al. [75]	Numerical analysis	Helically finned tubes	Syltherm 800 oil	373–573	933.7	72.5	3
Bellos et al. [76]	Numerical analysis	Internally finned absorber	Syltherm 800 oil	300–600	1000	69.18	1.27
Kalidasan et al. [72,73]	Experimental	Internal pin-fins	Water	304.65	400–450	39.12	30.97
Chakraborty et al. [77]	Numerical analysis	Helical absorber tube	Water	298–308	432–708	78.45	10
Bellos et al. [57]	Numerical analysis	Internally finned absorbers	Syltherm 800 oil	400–600	1000	68.80	0.82
Mwesigye et al. [66]	Numerical analysis	Perforated plate inserts	Syltherm 800 oil	400–650	1000	80.0	8
Yılmaz et al. [78]	Numerical analysis	wire coil inserts	Therminol-VP-1 oil	450–650	1000	77.9	1.4
Mwesigye et al. [79]	Numerical analysis	Wall-detached twisted tape inserts	Syltherm 800 oil	400–600	1000	87	10
Zheng et al. [47]	Numerical analysis	Porous insert	Steam	600	1000	68	4.2
Bozorg et al. [48]	Numerical analysis	Annular porous structure	Synthetic oil-Al$_2$O$_3$ nanofluid	500–600	1000	82.5	15
Present work	Numerical analysis	Inner tube and finned absorber	Syltherm 800 oil and water	400–600 and 298.15–318.15	300–1000	72.27	4.27

drawn as below.

(1) Analyses of velocity, temperature and heat flux distributions indicate that the FPTR-IT can successfully combine the advantages of FPTR and PTR-IT. The inner tube with low temperature HTF contributes to reducing the temperature and outward heat flux at the upper part of absorber, while the straight fins help to lower those at the lower part of absorber. As a result, the FPTR-IT obtains lower heat loss than that of the FPTR and smaller circumferential temperature difference than that of PTR-IT. In addition, the FPTR-IT can achieve the lowest temperature and heat loss of the absorber.

(2) Comprehensive comparisons with CPTR, FPTR and PTR-IT indicate that the FPTR-IT can always achieve the lowest maximum temperature and heat loss, and obtain the highest heat transfer of oil, PPC and total efficiency. Moreover, the Nusselt number of oil in FPTR-IT is enhanced by up to about 2.38 times that of CPTR and the maximum temperature of absorber in FPTR-IT is effectively reduced by up to 93.9 K.

(3) Performance evaluation under broad ranges of V_{oil} (50–250 L/min), $T_{in,oil}$ (400–600 K), and DNIs (300–1000 W/m^2) shows that the FPTR-IT can always obtain better performance than that of CPTR. Compared with CPTR, the heat loss of FPTR-IT is dramatically reduced by 9.9–148.1 W/m (20.7%–63.2%) and the total efficiency is effectively improved by 0.03%–4.27% at the studied conditions. Moreover, within the ranges of operating conditions herein, the proportions of heat gains for water and oil are ranged in 8.3%–73.9% and −12.0%–64.3%, respectively, while their

temperature gains are located in the range of 11.6–37.9 K and −1.2–19.6 K, respectively. The influences of V_{water} and $T_{in,water}$ are also investigated. The heat loss of FPTR-IT decreases slightly with the increasing V_{water} or decreasing $T_{in,water}$, while the total efficiency behaves the opposite trend.

1　Du S, Li Z Y, He Y L, et al. Experimental and numerical analysis of the hydraulic and thermal performances of the gradually-varied porous volumetric solar receiver. Sci China Tech Sci, 2020, 63: 1224–1234

2　He Y L, Qiu Y, Wang K, et al. Perspective of concentrating solar power. Energy, 2020, 198: 117373

3　Islam M T, Huda N, Abdullah A B, et al. A comprehensive review of state-of-the-art concentrating solar power (csp) technologies: Current status and research trends. Renew Sustain Energy Rev, 2018, 91: 987–1018

4　Hou H J, Wang M J, Yang Y P, et al. Performance analysis of a solar-aided power generation (SAPG) plant using specific consumption theory. Sci China Tech Sci, 2016, 59: 322–329

5　Zheng Z J, He Y L, Li Y S. An entransy dissipation-based optimization principle for solar power tower plants. Sci China Tech Sci, 2014, 57: 773–783

6　Han X, Xu C, Pan X Y, et al. Dynamic analysis of a concentrating photovoltaic/concentrating solar power (CPV/CSP) hybrid system. Sci China Tech Sci, 2019, 62: 1987–1998

7　Han X, Xu C, Ju X, et al. Energy analysis of a hybrid solar concentrating photovoltaic/concentrating solar power (CPV/CSP) system. Sci Bull, 2015, 60: 460–469

8　Zheng Y, Hatzell K B. Technoeconomic analysis of solar thermal desalination. Desalination, 2020, 474: 114168

9　Andrés-Mañas J A, Roca L, Ruiz-Aguirre A, et al. Application of solar

energy to seawater desalination in a pilot system based on vacuum multi-effect membrane distillation. Appl Energy, 2020, 258: 114068

10 Ahmadi M, Thimmaiah P, Bahrami M, et al. Experimental and numerical investigation of a solar eductor-assisted low-pressure water desalination system. Sci Bull, 2016, 61: 959–973

11 Zhang H, Shuai Y, Guene Lougou B, et al. Thermal characteristics and thermal stress analysis of solar thermochemical reactor under high-flux concentrated solar irradiation. Sci China Tech Sci, 2020, 63: 1776–1786

12 Cheng Z D, Leng Y K, Men J J, et al. Numerical study on a novel parabolic trough solar receiver-reactor and a new control strategy for continuous and efficient hydrogen production. Appl Energy, 2020, 261: 114444

13 Song C, Liu X L, Xuan Y M, et al. Granular porous calcium carbonate particles for scalable and high-performance solar-driven thermochemical heat storage. Sci China Tech Sci, 2021, 64: 2142–2152

14 Zhou X, Tian S, An J, et al. Modeling occupant behavior's influence on the energy efficiency of solar domestic hot water systems. Appl Energy, 2022, 309: 118503

15 Deng Y C, Quan Z H, Zhao Y H, et al. Experimental investigations on the heat transfer characteristics of micro heat pipe array applied to flat plate solar collector. Sci China Tech Sci, 2013, 56: 1177–1185

16 Wang F Q, Cheng Z M, Tan J Y, et al. Progress in concentrated solar power technology with parabolic trough collector system: A comprehensive review. Renew Sustain Energy Rev, 2017, 79: 1314–1328

17 Li L, Yu H J, Li Y S, et al. Characteristics of the transient thermal load and deformation of the evacuated receiver in solar parabolic trough collector. Sci China Tech Sci, 2020, 63: 1188–1201

18 Xiong Y X, Wu Y T, Ma C F, et al. Numerical investigation of thermal performance of heat loss of parabolic trough receiver. Sci China Tech Sci, 2010, 53: 444–452

19 Bellos E, Tzivanidis C. Alternative designs of parabolic trough solar collectors. Prog Energy Combust Sci, 2019, 71: 81–117

20 Manikandan G K, Iniyan S, Goic R. Enhancing the optical and thermal efficiency of a parabolic trough collector—A review. Appl Energy, 2019, 235: 1524–1540

21 Abdulhamed A J, Adam N M, Ab-Kadir M Z A, et al. Review of solar parabolic-trough collector geometrical and thermal analyses, performance, and applications. Renew Sustain Energy Rev, 2018, 91: 822–831

22 Ajbar W, Parrales A, Huicochea A, et al. Different ways to improve parabolic trough solar collectors' performance over the last four decades and their applications: A comprehensive review. Renew Sustain Energy Rev, 2022, 156: 111947

23 Wang Q, Shen B, Huang J, et al. A spectral self-regulating parabolic trough solar receiver integrated with vanadium dioxide-based thermochromic coating. Appl Energy, 2021, 285: 116453

24 Wang Q, Yang H, Zhong S, et al. Comprehensive experimental testing and analysis on parabolic trough solar receiver integrated with radiation shield. Appl Energy, 2020, 268: 115004

25 Bellos E, Tzivanidis C. Enhancing the performance of a parabolic trough solar collector with combined thermal and optical techniques. Appl Thermal Eng, 2020, 164: 114496

26 Zhao K, Jin H, Gai Z, et al. A thermal efficiency-enhancing strategy of parabolic trough collector systems by cascadingly applying multiple solar selective-absorbing coatings. Appl Energy, 2022, 309: 118508

27 Yang H, Wang Q, Zhong S, et al. Spectral-spatial design and coupling analysis of the parabolic trough receiver. Appl Energy, 2020, 264: 114692

28 Wang Q, Yang H, Hu M, et al. Optimization strategies and verifications of negative thermal-flux region occurring in parabolic trough solar receiver. J Cleaner Product, 2021, 278: 123407

29 Qiu Y, Xu Y, Li Q, et al. Efficiency enhancement of a solar trough collector by combining solar and hot mirrors. Appl Energy, 2021, 299: 117290

30 Qiu Y, Zhang Y, Li Q, et al. A novel parabolic trough receiver enhanced by integrating a transparent aerogel and wing-like mirrors. Appl Energy, 2020, 279: 115810

31 Li Q, Zhang Y, Wen Z X, et al. An evacuated receiver partially insulated by a solar transparent aerogel for parabolic trough collector. Energy Convers Manage, 2020, 214: 112911

32 Chavez Panduro E A, Finotti F, Largiller G, et al. A review of the use of nanofluids as heat-transfer fluids in parabolic-trough collectors. Appl Thermal Eng, 2022, 211: 118346

33 Hamzat A K, Omisanya M I, Sahin A Z, et al. Application of nanofluid in solar energy harvesting devices: A comprehensive review. Energy Convers Manage, 2022, 266: 115790

34 Tiwari A K, Kumar V, Said Z, et al. A review on the application of hybrid nanofluids for parabolic trough collector: Recent progress and outlook. J Cleaner Production, 2021, 292: 126031

35 Martínez-Merino P, Alcántara R, Gómez-Larrán P, et al. MoS_2-based nanofluids as heat transfer fluid in parabolic trough collector technology. Renew Energy, 2022, 188: 721–730

36 Bellos E, Tzivanidis C, Tsimpoukis D. Enhancing the performance of parabolic trough collectors using nanofluids and turbulators. Renew Sustain Energy Rev, 2018, 91: 358–375

37 Sandeep H M, Arunachala U C. Solar parabolic trough collectors: A review on heat transfer augmentation techniques. Renew Sustain Energy Rev, 2017, 69: 1218–1231

38 Liu W, Liu P, Wang J B, et al. Exergy destruction minimization: A principle to convective heat transfer enhancement. Int J Heat Mass Transfer, 2018, 122: 11–21

39 Fan A, Deng J, Guo Z, et al. A numerical study on thermo-hydraulic characteristics of turbulent flow in a circular tube fitted with conical strip inserts. Appl Thermal Eng, 2011, 31: 2819–2828

40 Huang Z, Li Z Y, Yu G L, et al. Numerical investigations on fully-developed mixed turbulent convection in dimpled parabolic trough receiver tubes. Appl Thermal Eng, 2017, 114: 1287–1299

41 Wang F Q, Lai Q Z, Han H Z, et al. Parabolic trough receiver with corrugated tube for improving heat transfer and thermal deformation characteristics. Appl Energy, 2016, 164: 411–424

42 Zhao Z, Bai F, Zhang X, et al. Experimental study of pin finned receiver tubes for a parabolic trough solar air collector. Sol Energy, 2020, 207: 91–102

43 Samiezadeh S, Khodaverdian R, Doranehgard M H, et al. CFD simulation of thermal performance of hybrid oil-Cu-Al_2O_3 nanofluid flowing through the porous receiver tube inside a finned parabolic trough solar collector. Sust Energy Technol Assess, 2022, 50: 101888

44 Kurşun B. Thermal performance assessment of internal longitudinal fins with sinusoidal lateral surfaces in parabolic trough receiver tubes. Renew Energy, 2019, 140: 816–827

45 Liu P, Lv J, Shan F, et al. Effects of rib arrangements on the performance of a parabolic trough receiver with ribbed absorber tube. Appl Thermal Eng, 2019, 156: 1–13

46 Sheikholeslami M, Said Z, Jafaryar M. Hydrothermal analysis for a parabolic solar unit with wavy absorber pipe and nanofluid. Renew Energy, 2022, 188: 922–932

47 Zheng Z J, Xu Y, He Y L. Thermal analysis of a solar parabolic trough receiver tube with porous insert optimized by coupling genetic algorithm and CFD. Sci China Tech Sci, 2016, 59: 1475–1485

48 Bozorg M V, Hossein Doranehgard M, Hong K, et al. CFD study of heat transfer and fluid flow in a parabolic trough solar receiver with internal annular porous structure and synthetic oil-Al_2O_3 nanofluid. Renew Energy, 2020, 145: 2598–2614

49 Liu P, Zheng N, Liu Z, et al. Thermal-hydraulic performance and entropy generation analysis of a parabolic trough receiver with conical strip inserts. Energy Convers Manage, 2019, 179: 30–45

50 Borunda M, Garduno-Ramirez R, Jaramillo O A. Optimal operation of a parabolic solar collector with twisted-tape insert by multi-objective genetic algorithms. Renew Energy, 2019, 143: 540–550

51 Peng H, Li M, Liang X. Thermal-hydraulic and thermodynamic performance of parabolic trough solar receiver partially filled with gradient metal foam. Energy, 2020, 211: 119046

52 Cheng Z D, He Y L, Cui F Q. Numerical study of heat transfer

enhancement by unilateral longitudinal vortex generators inside parabolic trough solar receivers. Int J Heat Mass Transfer, 2012, 55: 5631–5641

53 Sreenivasalu Reddy N, Gowreesh Subramanya S, Vishwanath K C, et al. Enhancing the thermal efficiency of parabolic trough collector using rotary receiver tube. Sust Energy Technol Assess, 2022, 51: 101941

54 Biswakarma S, Roy S, Das B, et al. Performance analysis of internally helically v-grooved absorber tubes using nanofluid. Thermal Sci Eng Prog, 2020, 18: 100538

55 Shi X, Zhao X, Wang F, et al. Improving overall heat transfer performance of parabolic trough solar receiver by helically convex absorber tube. Appl Thermal Eng, 2022, 213: 118690

56 Liu P, Wu J, Chen L, et al. Numerical analysis and multi-objective optimization design of parabolic trough receiver with ribbed absorber tube. Energy Rep, 2021, 7: 7488–7503

57 Bellos E, Tzivanidis C, Tsimpoukis D. Multi-criteria evaluation of parabolic trough collector with internally finned absorbers. Appl Energy, 2017, 205: 540–561

58 Liu P, Dong Z, Xiao H, et al. A novel parabolic trough receiver by inserting an inner tube with a wing-like fringe for solar cascade heat collection. Renew Energy, 2021, 170: 327–340

59 Song X, Dong G, Gao F, et al. A numerical study of parabolic trough receiver with nonuniform heat flux and helical screw-tape inserts. Energy, 2014, 77: 771–782

60 Nait-Ali B, Haberko K, Vesteghem H, et al. Preparation and thermal conductivity characterisation of highly porous ceramics. J Eur Ceramic Soc, 2007, 27: 1345–1350

61 Liu P, Dong Z, Xiao H, et al. Thermal-hydraulic performance analysis of a novel parabolic trough receiver with double tube for solar cascade heat collection. Energy, 2021, 219: 119566

62 Zhu X, Zhu L, Zhao J. Wavy-tape insert designed for managing highly concentrated solar energy on absorber tube of parabolic trough receiver. Energy, 2017, 141: 1146–1155

63 He Y L, Xiao J, Cheng Z D, et al. A MCRT and FVM coupled simulation method for energy conversion process in parabolic trough solar collector. Renew Energy, 2011, 36: 976–985

64 Mullick S C, Nanda S K. An improved technique for computing the heat loss factor of a tubular absorber. Sol Energy, 1989, 42: 1–7

65 Forristall R. Heat transfer analysis and modeling of a parabolic trough solar receiver implemented in engineering equation solver. Technical Report. NREL/TP-550-34169, National Renewable Energy Laboratory (NREL), 2003

66 Mwesigye A, Bello-Ochende T, Meyer J P. Heat transfer and thermodynamic performance of a parabolic trough receiver with centrally placed perforated plate inserts. Appl Energy, 2014, 136: 989–1003

67 ANSYS Inc. User's Guide for FLUENT/UNS and RAMPANT. Release 4.0, vol. 1, 2, and 4. Fluent Incorporated, Lebanon, NH 03766, 1996

68 Webb R L. Performance evaluation criteria for use of enhanced heat transfer surfaces in heat exchanger design. Int J Heat Mass Transfer, 1981, 24: 715–726

69 Incropera F P, Witt P D, Bergman T L, et al. Fundamentals of Heat and Mass Transfer. 6th ed. New York: John-Wiley & Sons Inc., 2006

70 Dudley E V, Kolb J G, Sloan M, et al. SEGS LS2 solar collector-test results. Report of Sandia National Laboratory, 1994, SAN94-1884

71 Kalidasan B, Shankar R, Srinivas T. Absorber tube with internal hinged blades for solar parabolic trough collector. Energy Procedia, 2016, 90: 463–469

72 Kalidasan B, Boopalan N, Shankar R, et al. Ameliorating heat transfer performance of absorber tube for single axis concentrators. Procedia Tech, 2016, 25: 924–933

73 Kalidasan B, Shankar R, Srinivas T. Absorber tube with internal pin-fins for solar parabolic trough collector. Asia Conference on Power and Electrical Engineering, 2016, 55: 06004

74 Chakraborty O, Roy S, Das B, et al. Computational analyses of parabolic trough solar collector in the presence of helical coil-insert. Int J Environ Sci Technol, 2023, 20: 683–702

75 Muñoz J, Abánades A. Analysis of internal helically finned tubes for parabolic trough design by CFD tools. Appl Energy, 2011, 88: 4139–4149

76 Bellos E, Tzivanidis C, Tsimpoukis D. Thermal enhancement of parabolic trough collector with internally finned absorbers. Sol Energy, 2017, 157: 514–531

77 Chakraborty O, Roy S, Das B, et al. Effects of helical absorber tube on the energy and exergy analysis of parabolic solar trough collector—A computational analysis. Sust Energy Technol Assess, 2021, 44: 101083

78 Yılmaz İ H, Mwesigye A, Göksu T T. Enhancing the overall thermal performance of a large aperture parabolic trough solar collector using wire coil inserts. Sust Energy Technol Assess, 2020, 39: 100696

79 Mwesigye A, Bello-Ochende T, Meyer J P. Heat transfer and entropy generation in a parabolic trough receiver with wall-detached twisted tape inserts. Int J Thermal Sci, 2016, 99: 238–257